OUR WARMING PLANET
TOPICS IN CLIMATE CHANGE

## Climate Lecture 4

# Atmospheric radiation

*Valdar Oinas*

NASA Goddard Institute for Space Studies, New York, NY.

Dr. Valdar Oinas (PhD in Astronomy from California Institute of Technology, 1971) is a senior research scientist at NASA Goddard Institute for Space Studies (GISS) in New York. Now fully retired from teaching physics at the CUNY Queensborough College in New York, Dr. Oinas has also been a member of the GISS climate modeling group since the mid-1970s. His chief area of expertise is the development of fast and accurate radiative transfer techniques to model solar and thermal radiation in the study of global climate change with applications also to remote sensing. He has been a key developer of the GISS GCM radiation modeling methodology

Imperial College Press,
2016

The climate system is well known for its great complexity and complex interactions that involve dynamic, thermodynamic, radiative, chemical, biological and human-driven processes. This view of the climate system has emerged from detailed measurements, meticulous record keeping, and theoretical analyses arising from, and made possible by the science and technology revolution that greatly advanced our understanding the role of physical processes that operate in the global climate system. These measurements also show very clearly that the global surface temperature has been rising over the past century, and that this is a consequence of human industrial activity.

***Key points***

Most basic are the near-daily measurements of surface air temperature at meteorological stations around the globe, some dating back to the 18th century. There are also precise measurements of the key atmospheric greenhouse gases ($CO_2$, $CH_4$, $N_2O$, $O_3$, CFCs) that are associated with fossil fuel burning and with other human industrial activities. Accurate monitoring of changes in solar irradiance and other radiative forcings that impact the climate system is likewise important. But these latter effects are small compared to the anthropogenic greenhouse gas forcings. The other important components of the scientific documentation of global climate change include field campaigns, theoretical studies, and laboratory analysis of climate constituent radiative properties.

Given the limited length of recorded climate data, and the complexity of the natural variability that is superimposed on the steadily increasing global warming component, statistical analyses of the measured data alone are not sufficient to establish a convincing cause-and-effect relationship between increasing atmospheric greenhouse gases and the increase in global surface temperature. Comprehensive general circulation climate models (GCMs) are needed to quantify, attribute, and fully understand the relative importance of the individual components of the climate system, and their role and contribution to the ongoing global warming and climate change.

Fortunately, a basic understanding of the ongoing global climate change does not require full knowledge of all physical processes that operate in the climate system. Conservation of energy is the overarching principle that constrains all of the changes that take place in the climate system. Absorbed solar energy (240 W/m$^2$ out of 340 W/m$^2$ global annual-mean incident solar energy) is virtually the entire source of energy input to the climate system. Other non-solar energy inputs to the climate system come from geothermal and tidal friction energy sources, and waste heat from nuclear energy and fossil fuel burning, together contribute approximately 0.1 W/m$^2$ to the global annual-mean energy budget, and are therefore of little consequence. This suggests then that atmospheric radiation is the key physical process that best describes the global energy balance of the Earth. Thus, the global-mean surface temperature of the Earth can be explained as being sustained by the steady input of absorbed solar shortwave (SW) heat-energy, warmed further by the greenhouse effect, and kept in energy balance by longwave (LW) thermal cooling to space.

The spectral distribution of the incident and reflected solar energy, and of the emitted longwave thermal energy to space, provides a full description of the global radiative energy balance. Given

the spatial distribution of water vapor, clouds, aerosols and other atmospheric gases, radiative analysis explains the surface temperature and thermal structure of the atmosphere. Convection and advection of heat also help define the atmospheric temperature structure, but such dynamic transports of energy are orders of magnitude slower than the radiative transports, and thus, do not directly interfere with, or otherwise impede, the radiative analysis of global energy balance.

***Nature of atmospheric radiation***

There are multiple aspects of electromagnetic radiation that are exceedingly complex. However, much of this complexity is not directly relevant to the radiative transfer modeling that is required for global climate studies. The key concepts that are needed to understand the nature of global warming and climate change are a working knowledge of the atmospheric greenhouse effect and of the radiative transfer modeling of heating by solar radiation and cooling by thermal emission. Explicit knowledge of the speed of light, particle-wave duality, or the probabilistic nature of quantum transitions, is not specifically required in climate-related applications (Petty, 2006).

Nevertheless, explicit numerical modeling of solar and thermal radiation is needed to determine the radiative heating and cooling rates at all points of the atmosphere and at the ground surface. This requires the differencing of height-resolved spectrally integrated solar and thermal fluxes, which need to be computed accurately. It is also important that the wavelength dependence of the spectral absorption and scattering by atmospheric constituents, and the angle dependence of the scattered and thermally emitted radiative fluxes be calculated accurately. For the absorbing gases in the atmosphere (e.g., water vapor, $CO_2$, and ozone), their spectral absorption consists of many thousands of individual absorption lines that need to be explicitly taken into account. Of equal importance is the angle dependence of both solar and thermal radiation since the amount of solar radiation heating the atmosphere depends on solar zenith angle, while atmospheric temperature gradients cause thermal radiation to depend on emission angle. Then too, solar radiation reflected by clouds, aerosols, and by the ground surface is characteristically angle dependent.

***Solar radiation***

Solar radiation illuminates the Earth in the form of an effectively parallel beam of radiative flux that delivers energy at the rate of 1360 W/m$^2$ referenced at the annual-mean Sun-Earth distance. This energy, averaged globally, is 340 W/m$^2$ of incident solar radiation. It is distributed over the spectrum from the UV to microwave wavelengths, with much of the energy residing at visible wavelengths. Solar energy arrives in minute energy packets (photons) containing energy $E = hv$, where $h$ is Planck's constant, $v$ is the frequency, which is related to the speed of light by $c = \lambda v$, where $\lambda$ is expressed in wavelength units. Basically, there are three things that can happen to incoming solar energy photons when they encounter an atmospheric constituent – they can be scattered, or absorbed, or continue forward in the original direction. Photons scattered upward into the upper hemisphere constitute *reflection*, while the photons scattered downward constitute *diffuse transmission*. Photons continuing in their original direction constitute *direct transmission*.

These options impart a probabilistic nature to atmospheric radiation modeling. The interaction strength with which atmospheric constituents interact with radiation is expressed by their spectral *optical depth* $\tau$ (a dimensionless ratio of constituent optical cross-section area relative to the area covered by the incident radiation). An optical depth of $\tau = 1$, implies an absorber (or a scattering agent) with a cross-section area that is just equal to the incident beam area (with the constituent compacted into a thin opaque layer perpendicular to the beam direction, without overlapping).

Radiative constituents are both exceedingly tiny and exceedingly numerous, and are randomly distributed along the light-beam path. In the mathematical limit as randomly distributed particles become ever smaller, convergence takes the form of the exponential function $\boldsymbol{exp}(-\tau)$, which accounts for the shadowing due to random particle overlap. This expression is recognized as the *direct beam transmission*. Without the random overlap, an absorber amount of $\tau = 1$ would have totally extinguished the incoming radiation beam. But, for randomly overlapping small particles of optical depth $\tau = 1$, significant transmission remains, and is given by $\boldsymbol{exp}(-1) = 0.368$.

***Mie scattering***

The wavelength and viewing-geometry dependence of atmospheric radiation can be complicated. But this dependence is actually well understood, and it can be included accurately and efficiently in climate modeling and remote sensing applications. Although requiring substantial computing effort, Mie theory is a very precise recipe for computing scattering of electromagnetic radiation by homogeneous spheres. Derived by Gustav Mie in 1908, it explains why scattering of light by atmospheric particulates is far more important for solar radiation than it is for thermal radiation. Because clouds are non-absorbing at visible wavelengths, they scatter visible light. But clouds are strongly absorbing at thermal wavelengths. The ratio of particle size to the wavelength of incident light determines the magnitude and wavelength dependence of particle scattering, and also the degree to which radiation is scattered in the forward direction. The key input parameters that define Mie scattering are the *particle size* and (wavelength dependent) *refractive index*.

For particles that are very small relative to the wavelength of light, Mie scattering efficiency is inversely proportional to the fourth power of the wavelength of the incident light. This scattering is also largely isotropic and is known as Rayleigh scattering. The prime example is scattering by air molecules that cause the characteristic blue sky color, since the shorter wavelengths are more strongly scattered relative to longer wavelengths. Cloud droplets (10 micrometers in radius) are significantly larger than the wavelength of visible light, so their scattering efficiency is largely independent of the wavelength, causing clouds to appear white. Another key characteristic of Mie scattering is that large particles tend to scatter light more efficiently in the forward direction compared to smaller particles. Aerosols (typically smaller than the wavelength), have scattering characteristics that are intermediate between Rayleigh scattering and scattering by clouds.

Mie scattering is computationally too intense to be performed directly in climate model radiative calculations. Instead, off-line calculations are made for a wide range of cloud particle sizes using

laboratory refractive indices that cover the entire spectrum from the UV to the microwave. It is variations in the imaginary part of the refractive index that determine the strength of cloud and aerosol wavelength dependent absorptivity. Absorptivity is near-zero at visible wavelengths for water, ice, and most aerosol compositions. Hence, these substances scatter visible light without absorbing it. Water, ice and aerosols have several absorption bands at near-IR wavelengths, and are strongly absorbing at most thermal wavelengths. Accurate modeling of the angle dependence of scattering by clouds and aerosols is the main concern when modeling solar radiation, while spectral absorption is the principal cloud and aerosol effect at thermal wavelengths.

Since cloud and aerosol particles interact with radiation at all wavelengths of the spectrum, Mie scattering calculations are tabulated to define the radiative parameters at all solar and thermal wavelengths. Specifically, the wavelength dependent radiative parameters are: (1) the *extinction efficiency factor*, $Q_x$, which is the ratio of the Mie extinction cross-section relative to the particle geometric cross-section, and can range from being much smaller than unity to as large as a factor of four; (2) the *single scattering albedo*, $\omega_o$, which is the non-absorbed fraction of light in a single scattering event ($\omega_o = 1$ for conservative scattering, $\omega_o = 0$ for total absorption); and (3) the *asymmetry parameter*, $g$; it defines the degree of forward scattering ($g = 1$, forward directed; $g = -1$, back directed; and $g = 0$, isotropically scattered). Derived from an exact electromagnetic theory and laboratory refractive indices, these radiative parameters serve as input to a radiative transfer model to calculate *multiple scattering* by atmospheric constituents and reflection by the ground surface. In climate GCMs, these calculations determine where solar radiation heats the atmosphere, how much is absorbed by the ground, and what fraction is reflected back to space.

***Multiple scattering of solar radiation***

An effective way to calculate multiply scattered atmospheric radiation is the energy-conserving doubling-and-adding algorithm described by Lacis and Hansen (1974). This algorithm accurately reproduces the spectral and angular dependence of Mie scattering results for clouds and aerosols for any specified optical depth, atmospheric distribution, and solar zenith angle geometry. The model also accounts for the absorption of solar radiation by atmospheric absorbing gases such as water vapor, ozone, and $CO_2$. Furthermore, the radiation model has the built-in capability to include or exclude *individual* scattering and absorbing constituents in prescribed combination. This enables the evaluation of each constituent's contribution to the total radiation budget by systematically evaluating the non-linear radiative interactions between the different radiative components. In performing such attribution for an annual-mean 1980 atmosphere, it is found that, about 30% of the incident solar radiation is reflected back to space, and of this, about 18% is by clouds, 7% by the ground surface, 4% by Rayleigh scattering, and about 1% by aerosols. Of the 70% of incident solar radiation that is absorbed by the Earth, about 50% is absorbed by the ground surface. About 20% is absorbed within the atmosphere, of which about 13% is absorbed by water vapor, 3% by clouds, 2% by ozone, and roughly 1% by oxygen and 1% by aerosols.

***Longwave thermal radiation and greenhouse effect***

Similar flux attribution can be performed for thermal longwave (LW) radiation. The land-ocean surface, water vapor, clouds, $CO_2$, and ozone are the principal emitters and absorbers of thermal radiation. Because of strong absorption by clouds and aerosols at thermal wavelengths, thermal radiation does not have to deal with the complexities of multiple scattering that are characteristic for solar radiation. With the global mean surface temperature being close to 288 K, the Planck radiation law requires that the longwave thermal flux emitted by the land-ocean surface must be about 390 W/m$^2$. For energy balance equilibrium, the global-mean outgoing longwave flux at the top of the atmosphere (TOA) must be 240 W/m$^2$ in order to balance the absorbed solar radiation. The 150 W/m$^2$ flux difference between the 390 W/m$^2$ emitted upward by the land-ocean surface and the TOA 240 W/m$^2$ going out to space is generated through the absorption and re-emission of thermal radiation by the atmospheric constituents. This 150 W/m$^2$ flux difference is a direct measure of the strength of the terrestrial greenhouse effect.

In attributing the 150 W/m$^2$, water vapor accounts for about 50% of the total greenhouse effect, longwave cloud opacity contributes about 25%, while the *non-condensing* greenhouse gases ($CO_2$, $CH_4$, $N_2O$, $O_3$, CFCs) account for the remaining 25%, with the strongest contributor $CO_2$, accounting for 20% (Lacis *et al.*, 2010). If the LW gaseous absorption and cloud opacity were to be removed from the atmosphere, strong surface cooling would ensue. Initially, the outgoing LW flux would be 390 W/m$^2$, a value not sustainable by the 240 W/m$^2$ of absorbed solar radiation. The global surface temperature would then drop rapidly to 255 K in order to maintain global energy balance. By partitioning of the LW flux contributors into *condensing* and *non-condensing* species, it becomes workable to infer a climate feedback sensitivity based only on the radiative structure of the atmosphere. This assessment follows because the atmospheric distribution of water vapor is established by fast feedback processes in which the condensation of water vapor is constrained by the temperature dependence of the Clauius-Clapeyron relationship. Accordingly, about 75% of the greenhouse effect is contributed by the fast feedback processes, while only 25% is due to radiative forcing by the non-condensing greenhouse gases. Hence, the direct radiative heating caused by the increase in atmospheric $CO_2$ is magnified by nearly a factor of three by the water vapor and cloud feedback effects. This makes atmospheric $CO_2$ the effective control knob that governs the global surface temperature of Earth (Lacis *et al.*, 2013).

***Technical issues***

The basic role of radiation in climate modeling is to calculate SW and LW radiative fluxes from which global energy balance and radiative heating and cooling of the atmosphere are determined. There are also important climate process details that add to the complexity of radiative modeling. Hygroscopic aerosols (e.g., sulfates, nitrates, and sea salt) change size in response to changes in relative humidity. Similarly, cloud particle size, optical depth and water/ice phase also change as meteorological conditions change. All of these changes have radiative consequences, and they affect the intensity and angle dependence of the scattered radiation. These effects are included in parameterized form in GCM radiation calculations. While the radiative effects of such structural changes may be small, they all need to be fully taken into account since the resulting changes in

particle size and refractive index cause the Mie scattering parameters to change, thus altering their cumulative radiative contributions to climate change forcing (Hansen and Travis, 1974).

Computational speed is a key constraint when performing climate model radiation calculations. The principal atmospheric absorbing gases ($H_2O$, $CO_2$, $O_3$) each have literally tens of thousands of spectral absorption lines spread over the spectrum. These absorption lines each have different strengths, with line-widths that are strongly dependent on atmospheric pressure and temperature. Line-by-line calculations are needed for accurate determination of their radiative contributions, but are prohibitively costly for climate modeling use. However, since only the spectral integral is actually needed, the absorption lines can be regrouped (off-line) according to absorption strength by using the correlated *k*-distribution approach (Lacis and Oinas, 1991). This approach, using angle dependent thermal emission, retains line-by-line precision at much reduced computing cost (Lacis *et al.*, 2013). Similarly, precise multiple scattering calculations of the solar zenith angle dependence of scattered radiation are prohibitively expensive to employ within a climate model. A single-quadrature version of the doubling-and-adding method was adapted to enable accurate calculation solar radiation multiple scattering in a climate modeling setting (Hansen *et al.*, 1983).

***Remote sensing applications***

Besides global energy balance and radiative heating and cooling rates, atmospheric radiation has another key role in remote sensing applications. Satellite observations of reflected solar radiation and emitted thermal radiation, including lidar, radar, and narrow spectral channel measurements, are used to determine the radiation balance of Earth, along with the retrieval of cloud and aerosol radiative properties, surface and atmospheric temperature, vegetation cover, water vapor, ozone, $CO_2$, and other absorbing gas distributions. All of this radiation-based satellite-measured climate system information has been used extensively in a comparative and diagnostic sense to test and evaluate climate model performance.

Typically, satellite remote sensing measurements utilize the variability of the *spectral intensity* (sometimes with very high spectral resolution) of the reflected solar radiation or emitted thermal radiation. This approach based on intensity-only measurements produces ambiguity (for aerosol radiative properties) because detectors cannot readily distinguish radiation scattered by aerosols from reflectivity by the ground surface, or due to sub-pixel cloud contamination. *Polarimetric* measurements provide an enhanced retrieval discrimination capability since radiation reflected from the ground surface tends to be unpolarized, while cloud and aerosol particles have distinct polarimetric signatures. This enabled Hansen and Hovenier [*1974*] to unambiguously identify the visible Venus cloud deck composition as 1 micrometer in radius sulfuric acid droplets. Similar polarimetric measurements were planned to retrieve quantitative aerosol information for Earth [*Mishchenko et al., 2007*], but the 2011 NASA *Glory* mission launch failure set back this plan.

**References**

Hansen, J.E., and J.W. Hovenier, 1974: Interpretation of the polarization of Venus. *J. Atmos. Sci.*, **31**, 1137–1160, doi:10.1175/1520-0469(1974).

Hansen, J.E., and L.D. Travis, 1974: Light scattering in planetary atmospheres. *Space Sci. Rev.*, **16**, 527–610, doi:10.1007/BF00168069.

Hansen, J., G. Russell, D. Rind, P. Stone, A. Lacis, S. Lebedeff, R. Ruedy, and L. Travis, 1983: Efficient three-dimensional global models for climate studies: Models I and II. *Mon. Weather Rev.*, **111**, 609–662, doi:10.1175/1520-0493(1983).

Lacis, A.A., and J.E. Hansen, 1974: A parameterization for the absorption of solar radiation in the Earth's atmosphere. *J. Atmos. Sci.*, **31**, 118–133, doi:10.1175/1520-0469(1974).

Lacis, A.A., and V. Oinas, 1991: A description of the correlated k distributed method for modeling nongray gaseous absorption, thermal emission, and multiple scattering in vertically inhomogeneous atmospheres. *J. Geophys. Res.*, **96**, 9027–9063, doi:10.1029/90JD01945.

Lacis, A.A, G.A. Schmidt, D. Rind, and R.A. Ruedy, 2010: Atmospheric $CO_2$: Principal control knob governing Earth's temperature. *Science*, **330**, 356–359, doi:10.1126/science.1190653.

Lacis, A.A., J.E. Hansen, G.L. Russell, V. Oinas, and J. Jonas, 2013: The role of long-lived greenhouse gases as principal LW control knob that governs the global surface temperature for past and future climate change. *Tellus B*, **65**, 19734, doi:10.3402/tellusb.v65i0.19734.

Mishchenko, M.I., 2009: Gustav Mie and the fundamental concept of electromagnetic scattering by particles: A perspective. *J. Quant. Spectrosc. Radiat. Transfer*, **110**, 1210–1222, doi:10.1016/j.jqsrt.2009.02.002.

Mishchenko, M.I., B. Cairns, G. Kopp, C.F. Schueler, B.A. Fafaul, J.E. Hansen, R.J. Hooker, T. Itchkawich, H.B. Maring, and L.D. Travis, 2007: Accurate monitoring of terrestrial aerosols and total solar irradiance: Introducing the Glory mission. *Bull. Amer. Meteorol. Soc.*, **88**, 677–691, doi:10.1175/BAMS-88-5-677.

Petty, G.W., 2006: *A First Course in Atmospheric Radiation*, Sundog Publishing, Madison, WI, 459 pp.

Tang, I.N., W.T. Wong, and H.R. Munkelwitz, The relative importance of atmospheric sulfates and nitrates invisibility reduction, *Atmospheric Environment*, **15**, 2463–2471, 1981.

Tang, I.N. and H.R. Munkelwitz, Simultaneous determination of refractive index and density of an evaporating aqueous solution droplet, *Aerosol Sci. and Tech*, **15**, 201–207, 1991.

Tang, I.N. and H.R. Munkelwitz, Water activities, densities, and refractive indices of aqueous sulfates and sodium nitrate droplets of atmospheric importance, *J. Geophs. Res.*, **99**, 18801–18808, 1994.

**Slide 1**

**Our Warming Planet: Topics in Climate Change**

A Compendium of Lectures on Special Topics
in Climate Dynamics and Climate Change

*A Tribute to David Rind*
*for Outstanding Climate Science Achievements*

# Atmospheric Radiation

*Valdar Oinas*
NASA Goddard Institute for Space Studies

Imperial College Press
2016

**Slide 2**

## Spectral Distribution and Global Attribution of Solar SW Radiation

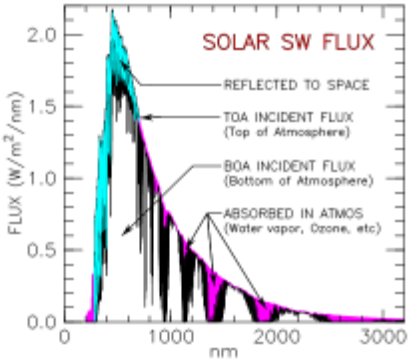


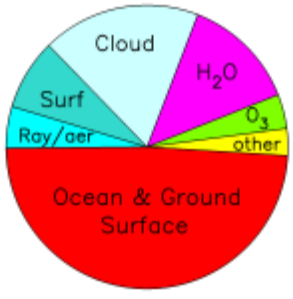


Solar radiation is the ultimate source of energy that supports the temperature structure of the terrestrial climate system.

**Slide 3**

## Spectral Distribution & Forcing/Feedback Attribution of Thermal Radiation

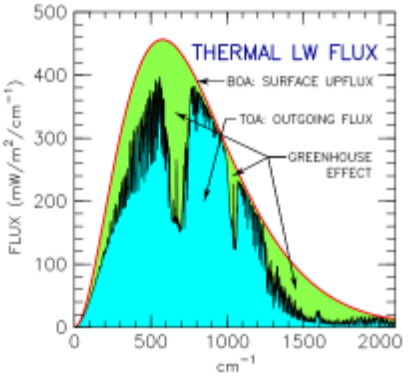


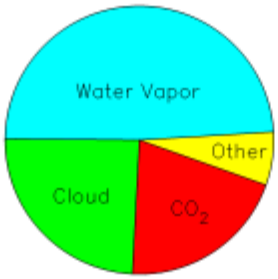


Top of atmosphere (TOA) spectral distribution of the outgoing thermal radiation emitted by Earth (left panel). By means of radiative modeling attribution (right-hand pie chart), it can be shown that water vapor accounts for nearly 50% of the terrestrial greenhouse effect, with clouds contributing about 25%, $CO_2$ about 20%, and the minor GHGs ($CH_4$, $N_2O$, $O_3$, CFCs) the remaining 5%.

*Oinas, V.* **Atmospheric Radiation** 3

**Slide 4**

## Mie Scattering Size Dependence & Relative Spectral Extinction

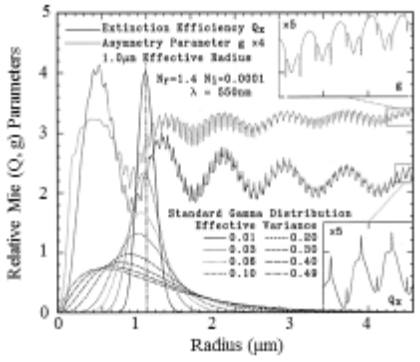


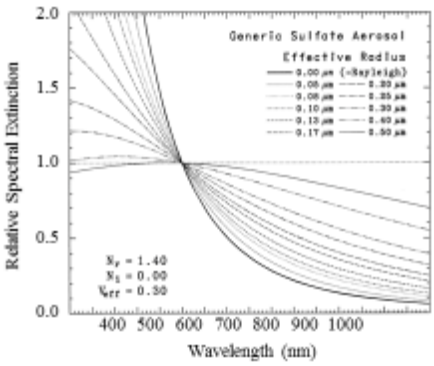


Optical properties (scattering, absorption) of atmospheric aerosols are a function of the size of the particle and the wavelength of the radiation.

*Oinas, V.* **Atmospheric Radiation** 4

**Slide 5**

## Spectral Refractive Index of Liquid Water & Ammonium Sulfate

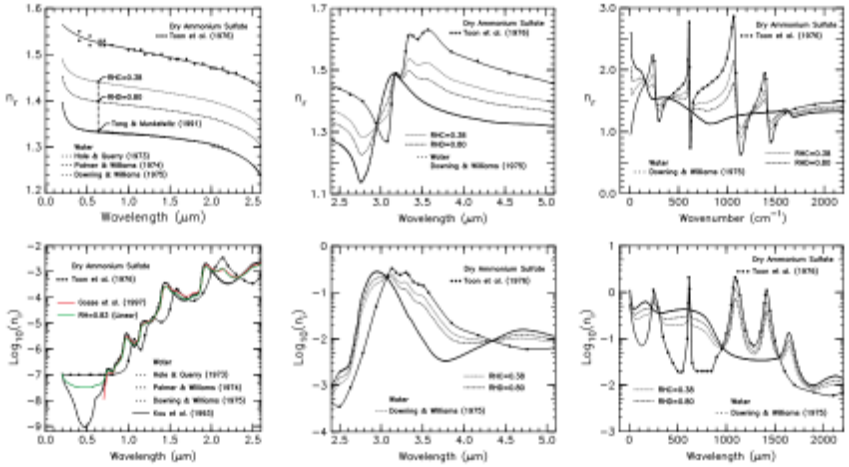


Spectral dependence of real (top panels) and imaginary (bottom panels) refractive index components for liquid water, dry ammonium sulfate, and relative humidity dependent sulfate solute at visible, near-IR, and far-IR wavelengths.

*Oinas, V.* **Atmospheric Radiation** 5

**Slide 6**

## Mie-Scattering & T-Matrix Cloud Radiative Parameters for Ice

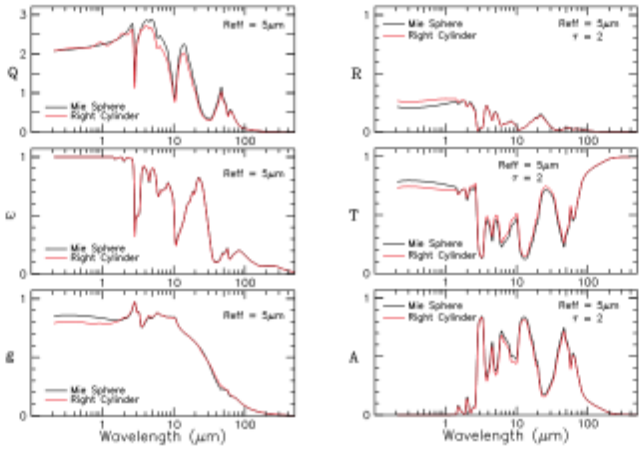


Optical properties of ice clouds as a function of the wavelength of the radiation.

*Oinas, V.* **Atmospheric Radiation** 6

**Slide 7**

## Cloud, Ozone, & Dust Radiative Effect on Solar SW Spectral Reflectivity

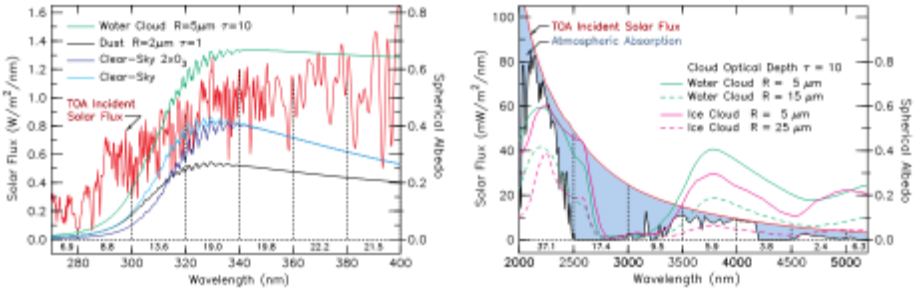


Radiative effects of cloud, ozone, and mineral dust on the spectral dependence of reflected solar SW radiation.



**Slide 8**

## Cloud Optical Depth & Sun-Angle Effect on Total-Spectrum SW Albedo

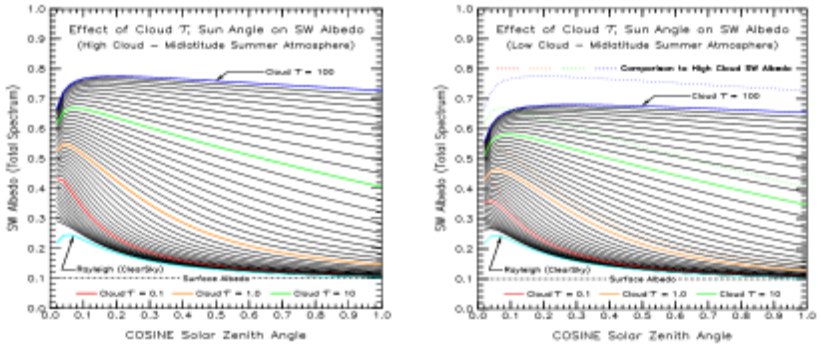


Total-spectrum SW albedo dependence on cloud optical depth, solar zenith angle, and cloud height.

**Slide 9**

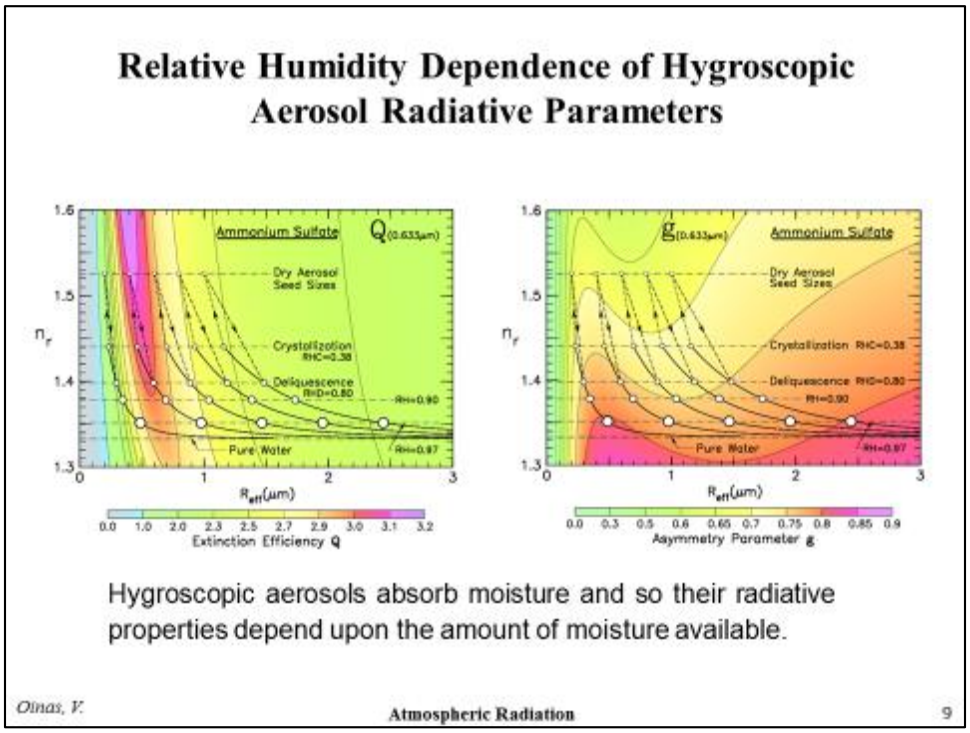


**Slide 10**

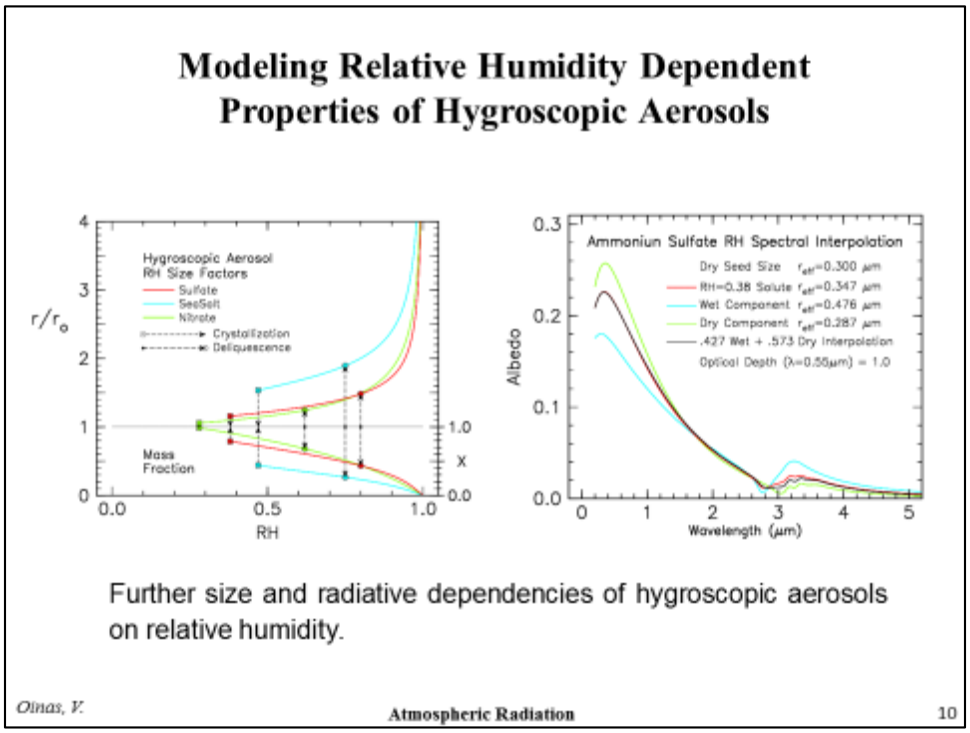

**Slide 11**

## Mie Scattering Parameters for Sulfate & Mineral Dust Aerosol

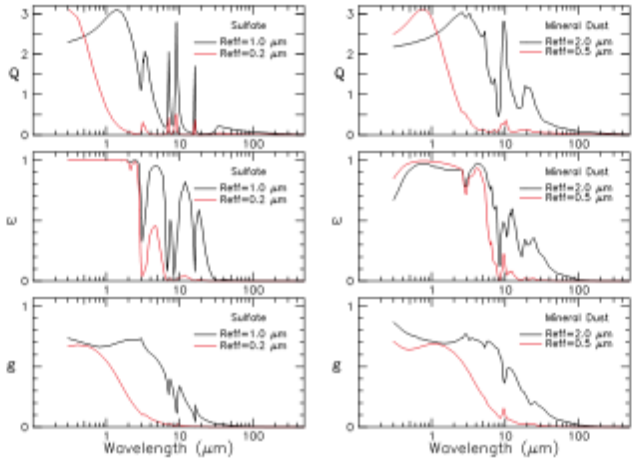


Mie scattering of aerosols as a function of their size displays a complex relationship.



**Slide 12**

## Reflection, Transmission, Absorption for Sulfate & Mineral Dust

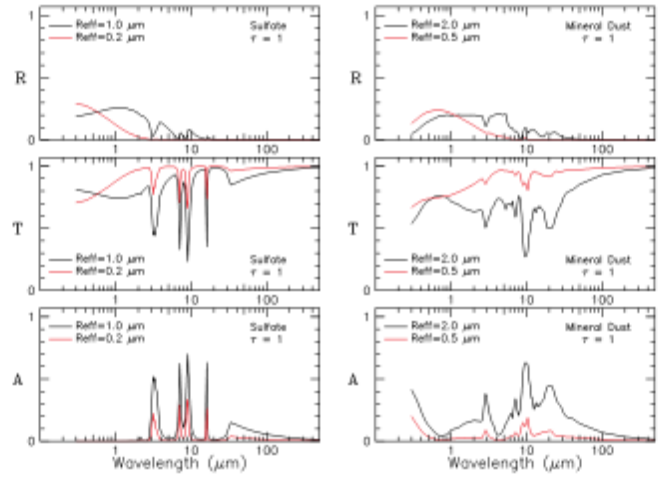


Similarly, the impact of aerosols on atmospheric radiation is a complicated function of aerosol size and radiative wavelength.

**Slide 13**

## Physical Basis for Thermal Radiation Emission, Absorption, Transmission

Kirchhoff's Law and the isothermal cavity concept provide a convenient starting point to develop the radiative transfer formulations needed to calculate and model the emission, absorption, and transmission of thermal radiation.

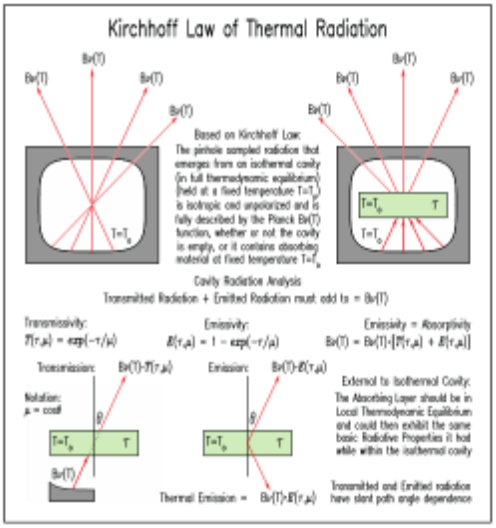




**Slide 14**

## Line-by-Line Calculation of LW Spectral Fluxes and Radiative Cooling Rate

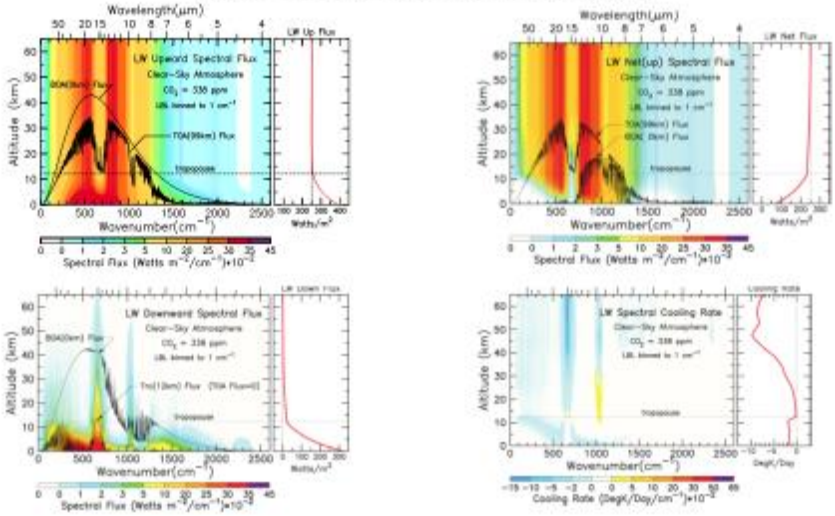


Line-by-Line $CO_2$ spectral fluxes and radiative and radiative cooling rate profiles.

**Slide 15**

## Converting $CO_2$ Line Spectrum into Correlated *k*-Distribution Form

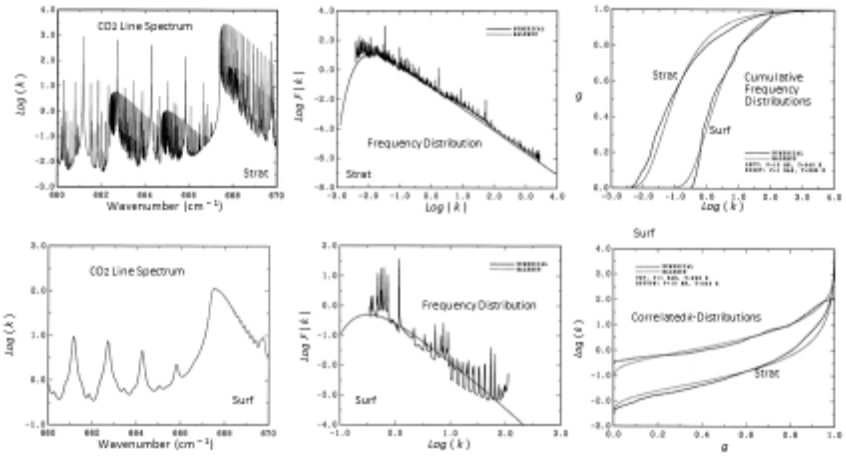


The line by line absorption pattern for $CO_2$ has to be parameterized for use in the GCM.



**Slide 16**

## Malkmus Model Utilization in Formulating the Correlated *k*-Distribution

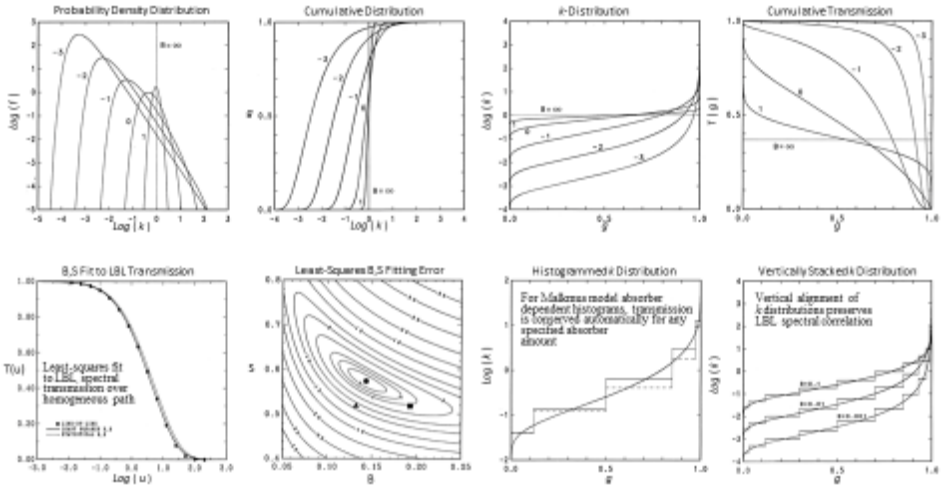


The Malkmus Model is used for this parameterization.

**Slide 17**

## Effect of Cloud Optical Depth on Angle Dependence of LW Radiation

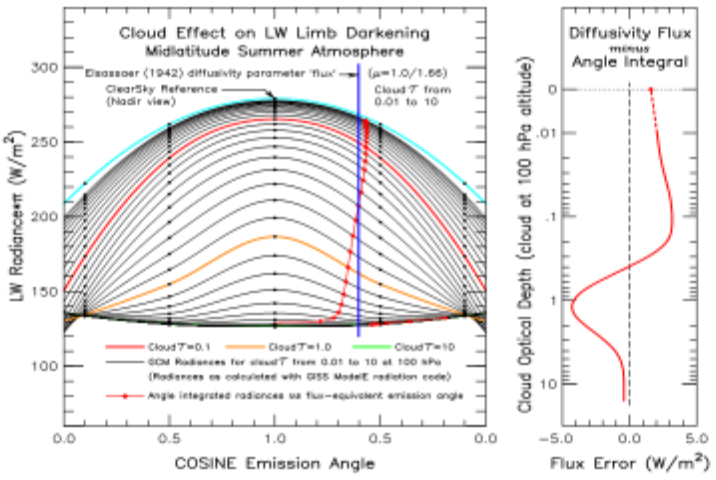


The thermal radiation emitted by Earth is view-angle dependent due to the vertical atmospheric temperature gradient.

*Oinas, V.* **Atmospheric Radiation** 17

**Slide 18**

## Parameterizing LW Cloud Scattering Effects on LW TOA & BOA Fluxes

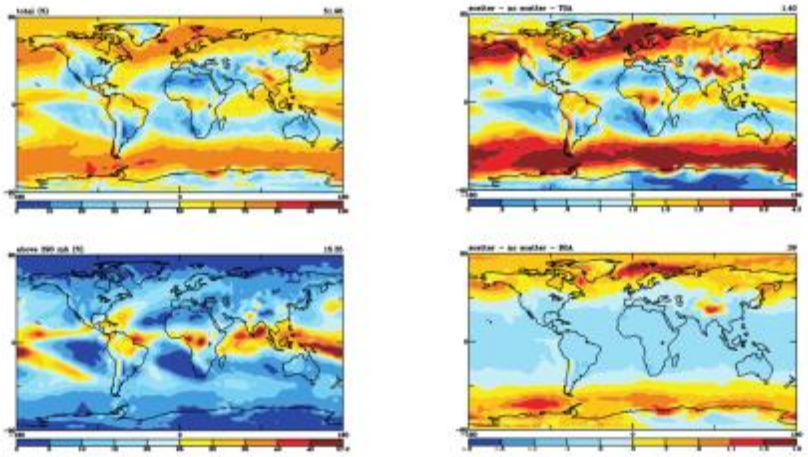

Results of the parameterized calculation of the effects of cloud scattering on longwave radiation at the top of the atmosphere (TOA) and bottom of the atmosphere (BOA).

*Oinas, V.* **Atmospheric Radiation** 18

**Slide 19**

## Polarimetric Scattering-Angle Signature: Set by Size and Refractive Index

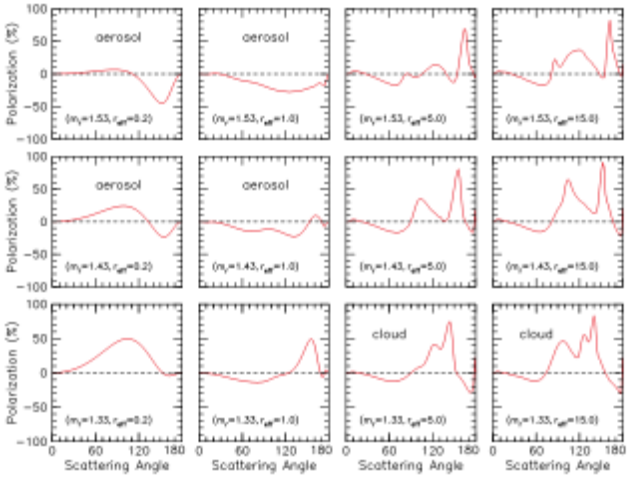


The polarization of light by atmospheric aerosols and clouds is a function of particle size and refraction index.

*Oinas, V.* **Atmospheric Radiation** 19

**Slide 20**

## Performance Capability of Polarimetry in Remote Sensing Applications

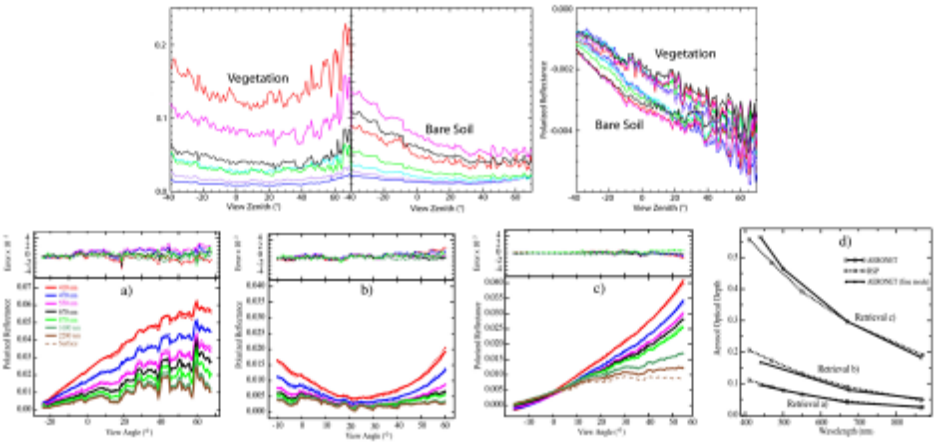


Observations of the polarization properties of reflected light can help determine characteristics of the reflecting features.

*Oinas, V.* **Atmospheric Radiation** 20

# Slide Notes

**Slide 2** Spectral distribution of incident solar radiation (left-hand panel) with indicated clear-sky spectral reflection due to atmospheric Rayleigh scattering (blue) and absorption (magenta) by water vapor, oxygen and ozone. Solar radiation is the ultimate source of energy that supports the temperature structure of the terrestrial climate system. Globally-averaged, the annual-mean incident solar radiation is about 340 W/m$^2$. As shown in the (right-hand) pie-chart, about 30%, or 100 W/m$^2$, is reflected directly back to space primarily by clouds, Rayleigh scattering, aerosols, and by the ocean, land, and snow/ice surfaces, leaving a net 240 W/m$^2$ as the heat energy input to the terrestrial climate system. Approximately 20% (70 W/m$^2$) of the incident solar radiation is absorbed within the atmosphere, primarily by water vapor, but also by ozone, clouds, aerosols, $O_2$, $CO_2$ and other minor atmospheric gases. Roughly half of the incident solar radiation is absorbed by the ocean and land surface. The result shown are from a reference 1980 atmosphere.

The Sun has been a remarkably steady source of energy over all of recorded history. Decades of precise measurements show a 0.1% variability associated with the 11-year sun-spot cycle. There is also a seasonal cycle in solar irradiance due to Earth's orbital eccentricity such that the incident solar energy in January is about 3.4% greater than the annual mean, and 3.4% less in July, even though the global temperature is about 4 °C warmer in July than in January. The normal-incident solar radiation at the mean Sun-Earth distance is 1360.8 W/m$^2$ (Kopp and Lean, 2011).

**Slide 3** Top of atmosphere (TOA) spectral distribution of the outgoing thermal radiation emitted by Earth (left panel). The annual-mean globally-mean LW thermal flux emitted upward by the ground (surface temperature 288 K) is about 390 W/m$^2$ (red line). The blue area depicts the spectral distribution of the outgoing LW thermal radiation emitted to space by the Earth (about 240 W/m$^2$). This is expected for global energy balance with the 240 W/m$^2$ of absorbed SW solar radiation. The flux difference of 150 W/m$^2$ (green area) between the upwelling LW flux at ground surface and outgoing LW flux at TOA is a measure of the strength of the terrestrial greenhouse effect. It is not a simple atmospheric transmission effect, arising instead from a series of absorption and emission events which depend on the spectral absorption strength and occur throughout the atmosphere.

This 150 W/m$^2$ greenhouse effect is due entirely to the LW spectral absorption by the atmospheric greenhouse gases and by the spectral cloud opacity. By means of radiative modeling attribution (right-hand pie chart), it can be shown that water vapor accounts for nearly 50% of the terrestrial greenhouse effect, with clouds contributing about 25%, $CO_2$ about 20%, and the minor GHGs ($CH_4$, $N_2O$, $O_3$, CFCs) the remaining 5%. This also shows that $CO_2$ and the minor GHGs represent the radiative forcings of the climate system(since they remain in the atmosphere virtually indefinitely once injected), while water vapor and clouds are the fast feedback effects of the climate system changing in response to local meteorological conditions. Thus, in the terrestrial atmosphere, feedback effects multiply the direct $CO_2$ or GHG greenhouse radiative forcing by about a factor of three.

**Slide 4** Mie scattering extinction efficiency (***Qx***) and asymmetry (***g***) parameter dependence on particle size. Scattering of electromagnetic radiation by homogenous spherical particles is remarkably complex. As the particle changes minutely in size, there is changing interference between light transmitted though the particle, refracted around the particle, and light reflected internally within the particle, to produce the low frequency and high frequency fluctuations in ***Qx*** and ***g*** (shown magnified by a factor of 5 in the left-hand inset). Extinction efficiency ***Qx*** is the ratio of the Mie scattering cross-section relative to the particle's geometric area, ranging from zero in the small particle limit to as large as a factor of 4. The asymmetry parameter ***g*** is similarly near-zero in the small particle limit, approaching unity in the large particle limit (multiplied by a factor of 4 in the figure). In Mie scattering, the particle size (R) and wavelength ($\lambda$) of the scattered light are reciprocally related through the ratio $X = 2\pi R/\lambda$. In practice, cloud and aerosol particles are never found to be mono-modal, being described instead by a particle size distribution (e.g. standard Gamma) characterized by an effective radius Reff and effective variance Veff.

The right-hand panel shows the relative spectral dependence of the Mie extinction efficiency ***Qx*** for typical sulfate aerosol particles ranging from near-zero to 0.5 μm in size, with a moderately broad effective variance of Veff = 0.3. At near-zero size, aerosol particles exhibit the strong $\lambda^{-4}$ (blue-sky) Rayleigh spectral dependence. As particle size increases beyond Reff = 0.5 μm, spectral extinction becomes increasingly flatter (and whiter).

**Slide 5** Spectral dependence of real (top panels) and imaginary (bottom panels) refractive index components for liquid water, dry ammonium sulfate, and relative humidity dependent sulfate solute at visible, near-IR, and far-IR wavelengths. Radiative properties of solids and liquids are defined by their complex refractive index. The real part of the refractive index ***nr*** refers to overall substance refractivity, the imaginary part ***ni*** describes the degree of absorption. For typical substances, ***nr*** tends to vary slowly across visible wavelengths, exhibiting spectral features that are associated with absorption bands in the near and far-IR spectral regions. The imaginary refractive index is small in the visible for both water and sulfate, increasing in strength and variability toward the infrared. Laboratory data are the basic source of refractive index information. Particle size and the complex refractive index are the key input parameters to Mie scattering calculations needed to compute cloud and aerosol radiative properties.

**Slide 6** Spectral dependence of Mie-scattering (spherical) and T-matrix (non-spherical) radiative parameters ($Q_x$, $\omega_o$, $g$) for 5 μm ice-cloud particles (left-hand panels). Mie scattering is an exact theory for spherical particles. T-matrix is an exact theory for randomly oriented non-spherical particles, and is depicted here for 5 μm effective-radius equivalent-sphere right cylinders with a 1:1.5 aspect ratio. The principal effect of particle non-sphericity is a decrease in forward scattering, manifested by decreased asymmetry parameter $g$ for wavelengths shortward of 2 μm, resulting in enhanced reflectivity and decreased transmission of SW radiation (right-hand panels). This is also the spectral region of essentially zero absorption by cloud particles. A doubling/adding radiative transfer model is used to convert the input ($Q_x$, $\omega_o$, $g$) radiative parameters into the physically more relevant (R,T,A) reflection, transmission, and absorption information.

**Slide 7** Radiative effects of cloud, ozone, and mineral dust on the spectral dependence of reflected solar SW radiation. The left-hand scale of the left panel depicts the spectral variation of solar flux in the UV part of the spectrum (red curve). The Spherical Albedo scales on the right side of the figures depict the fraction of the incident solar radiation as function of wavelength (integrated over solar zenith angle) that is reflected back to space. Most evident in the UV is the strong absorption by ozone. UVA radiation (340-400 nm) is scarcely affected by ozone, while the UVC radiation (<290 nm) is so strongly absorbed that scarcely any reaches the ground. On the other hand, UVB radiation is modulated by ozone amount as indicated by the dark-blue curve for doubled O3 relative to the clear-sky Rayleigh scattering. The green curve depicts the spectrally steady reflectivity (>340 nm) of a typical ($\tau$ = 10) water cloud, with little dependence on particle size or cloud height. By comparison, absorption by ($\tau$ = 1) desert dust results in less reflection than the clear-sky Rayleigh scattering case.

In the near-IR (right-hand panel), the spectral dependence of reflected radiation is more complicated. Within the gray areas, there is strong absorption by water vapor and CO2, so little of the incident radiation is reflected. But there are significant "window" regions (2000-2500 nm, and 3500-4000 nm) where clouds have opportunity to reflect some of the incident solar radiation. However, because clouds exhibit some absorptivity in the near-IR spectral region, the cloud radiative parameters become more sensitive to particles size since for larger particles there is more opportunity for light traversing the particle to be absorbed, than is the case for smaller particles. Also, in the near-IR, there is a substantial dependence of cloud reflectivity on water/ice phase. In the visible spectrum where cloud absorption is small, the light path difference has a much smaller radiative effect.

**Slide 8** Total-spectrum SW albedo dependence on cloud optical depth, solar zenith angle, and cloud height. The left-hand panel shows the reflected spectrally integrated SW flux at the top of the atmosphere (plane albedo) as a function of the solar zenith angle (sun-rise to direct over-head), calculated with the GISS ModelE radiation code for high-cloud (cirrus) optical depth ranging from near-zero ($\tau$=0.01) to optically extreme ($\tau$=100). For reference, the blue-green line at the bottom is for clear-sky Rayleigh scattering. The cloud optical depth is logarithmically incremented with the decadal values ($\tau$=0.1, 1, 10, 100) identified by the red, orange, green, and blue lines, respectively. What is evident is the strong solar zenith angel dependence for small optical depths which gradually flattens out as cloud optical depth increases. Of note is the marked decrease in reflectivity at low sun angles, caused by increased ozone absorption along an increasing atmospheric path.

The right-hand panel displays the same basic results as the left-hand panel, except that the cloud is located at low altitude near ground level. The difference now is that the tropospheric gases, primarily water vapor, are located above the cloud, and are able to absorb the incident radiation on its way down, as well as the reflected radiation on its way up. The colored dotted lines corresponding to the decadal optical depth values quantify the amount of this absorption.

**Slide 9** Relative humidity dependence of ammonium sulfate Mie scattering (***Qx***,***g***) radiative parameters according to laboratory measurements (at 0.633 μm) by Tang and Munkelwitz [*1991*, *1994*, *1996*]. The left-hand panel is a color-contour grid of the Mie scattering extinction efficiency parameter (***Qx***) calculated for refractive indices (***nr***) and particle sizes (***Reff***) as shown. Superimposed on this grid are parametric curves

relating the refractive index and particle size measured for a suspended ammonium sulfate droplet as relative humidity undergoes change. The sulfate aerosol exhibits hysteresis behavior by remaining "dry" until a deliquescence relative humidity is reached (RHD=0.80), whereupon it then rapidly takes on moisture to become a solute, and moves along the equilibrium curve, changing in size as relative humidity changes. If the relative humidity falls below the critical crystallization value (RHC=0.38), the solute rapidly loses its remaining moisture to become a dry particle again.

Similarly, the right-hand panel is the Mie scattering asymmetry parameter (***g***) grid, superimposed on which are the parametric curves that relate the refractive index and particle size dependence on relative humidity for the sulfate aerosol droplet. In this way, the Mie-scattering ***Qx***(***nr***,***Reff***) and ***g***(***nr***,***Reff***) grids serve as look-up tables for the Tang and Munkelwitz (***nr***,***Reff***,***RH***) parametric formulations to enable rapid determination of the (***Qx***,***g***) radiative parameters for any dry-size sulfate aerosol as a function of changing relative humidity.

**Slide 10** Hygroscopic aerosol size and (dry) mass fraction as functions of relative humidity. Size, density, and refractive index of hygroscopic aerosols follows a hysteresis loop as has been shown by laboratory measurements for sulfate, sea salt, and nitrate aerosols [*Tang and Munkelwitz 1991, 1994, 1996*]. As shown in the left-hand panel, when relative humidity (RH) reaches the deliquescence point (filled circles), the dry aerosol particles rapidly take on moisture to become solute particles. They then follow the equilibrium curves for the respective species, changing in size as RH changes. If RH decreases below the crystallization point (filled squares), the solute droplets rapidly lose their remaining moisture and drop from the equilibrium curve.

The right-hand panel demonstrates how RH dependent radiative parameters for a hygroscopic aerosol can be parameterized. The (reference) red curve utilizes Mie scattering parameters computed for the appropriate solute spectral refractive index at RH=0.38, clearly an *internally* mixed aerosol composition. The black line depicts the spectral albedo computed for an *externally* mixed aerosol comprised of *dry sulfate* and *pure water* components. Thus, the radiative properties for an originally 0.300 μm dry sulfate aerosol (which becomes a 0.347 μm solute particle at RH=0.38) can be accurately represented as the weighted average of a pure dry 0.287 μm dry sulfate particle and a 0.476 μm pure water aerosol, with the dry sulfate and pure water sizes and fractional amounts selected to match match the (***Qx***,***g***) of the solute sulfate aerosol. This parameterization simplifies the tabulated input data needed for computing the radiative effects of hygroscopic aerosols.

**Slide 11** Spectral dependence of Mie Scattering parameters (***Q***,$\omega$,***g***) for representative 0.2 and 1.0 μm sulfate aerosol (left-hand panels), and for 0.5 and 2.0 μm mineral dust aerosols (right-hand panels). The extinction efficiency parameter ***Q*** is the ratio of the Mie scattering cross-section relative to the particle's geometric cross-section. It varies with wavelength because the sulfate refractive index varies with wavelength. The spectral features are co-aligned in wavelength, but notably, the Mie size dependence is non-linear. The single scattering albedo $\omega$ is a measure of aerosol absorptivity with $\omega$ = 1.0 indicating no absorption, and $\omega$ = 0 indicating total absorption. The asymmetry parameter ***g*** is a measure of the degree of forward scattering. The right-hand panel illustrates similar Mie Scattering (***Q***,$\omega$,***g***) parameters for mineral dust particles. The differing spectral refractive indices are the means for aerosol composition retrieval.

**Slide 12** Reflection, transmission, and absorption for unit optical depth based on the appropriate Mie Scattering parameters ($\boldsymbol{Q},\boldsymbol{\omega},\boldsymbol{g}$) for 0.2 and 1.0 μm sulfate aerosol (left-hand panels), and 0.5 and 2.0 μm mineral dust aerosol (right-hand panels). The spectral radiative transfer calculations are performed using the doubling/adding method. The notable characteristics are that sulfate aerosol is basically non-absorbing for wavelengths shortward of 3 μm, while mineral dust exhibits substantial SW absorption, significantly stronger for the larger particle size and increasing toward the blue. Also notable are the four prominent sulfate aerosol absorption features in the mid-thermal spectral region. By comparison, the LW absorption by mineral dust has significantly broader absorption bands. Also of further note is the substantial reflectivity by the 2.0 μm mineral dust in the near-IR, and extending longward to the 10-30 μm region.

**Slide 13** Kirchhoff's Law and the isothermal cavity concept provide a convenient starting point to develop the radiative transfer formulations needed to calculate and model the emission, absorption, and transmission of thermal radiation. Basically, the radiation field inside an isothermal cavity is Planck radiation at temperature To of the isothermal cavity. Sampling the cavity radiation by means of arbitrarily positioned pinholes will all yield the same Planck intensity B(To). If an absorbing slab of optical depth $\tau$ and temperature T=To is inserted into the cavity, Kirchhoff's Law maintains that the radiation sampled through the pinholes will yield the same Planck intensity B(To). Since the thermal emission from the inner surface of the isothermal cavity must be B(To), it follows that transmissivity, emissivity, and absorptivity must be related as shown in the figure in order that the pinhole radiation maintain its Planck intensity B(To). The radiation field inside the isothermal cavity being in thermodynamic equilibrium serves also to define the absorption coefficients and the optical depth consistent with the prevailing pressure-temperature conditions in the cavity. In the outside world, under slowly changing temperature gradients, local thermodynamic equilibrium closely approximates thermodynamic equilibrium.

**Slide 14** Line-by-Line CO2 spectral fluxes and radiative and radiative cooling rate profiles. Top-left panel shows LW up flux, and bottom-left panel shows the down flux for 338 ppm CO2 concentration. The top-right panel depicts the net upward LW flux. The incremental change in the net flux profile with height defines the vertical profile of the radiative cooling rate shown in the bottom-left panel. Water vapor is the principal cooling gas in the troposphere. CO2 cooling dominates in the stratosphere, but water vapor and ozone also contribute.

**Slide 15** Top left panel depicts the line-by-line (LBL) absorption coefficient spectrum from near-center (660-670 $cm^{-1}$) of the 15 μm CO2 band for a pressure of 10 hPa and temperature 240 K. The bottom left panel displays the same spectral region but for a pressure of 1000 hPa and temperature 296 K. Pressure broadening accounts for the marked difference between the two spectra. Central panels depict frequency distributions $\boldsymbol{F(k)}$ of corresponding LBL spectra. Superimposed are Malkmus band model frequency distributions that closely reproduce the LBL spectral transmission. The top right-hand panel depicts the cumulative frequency distributions $\boldsymbol{g}$ of both LBL and Malkmus model frequency distributions displayed in the central panels. Inverting the axis of the cumulative frequency distributions produces the corresponding *k*-distributions shown in the bottom right-hand panel. There are no substantial

approximations in converting the LBL spectra to *k*-distributions. For a homogeneous path, both methods reproduce the same 660-670 $cm^{-1}$ spectrally integrated transmission. Since line positions do not change with pressure, Stratospheric and Surface *k*-distributions remain strongly correlated as functions of ***g***.

**Slide 16** The Malkmus band model is a convenient analysis tool well-suited for numerical manipulation of the correlated *k*-distribution. This is because analytic 2-parameter formulations exist for the probability density ***f***, cumulative fraction ***g***, inverse ***k*** distributions, and the corresponding transmission (top-row panels), derived specifically for randomly overlapping Lorentz-line spectra with exponential line strength distribution. The Malkmus $\boldsymbol{B} = b/d$, and $\boldsymbol{S} = s/d$, parameters (where $b,s,d$ are spectral line mean half-width, strength, and line spacing) provide a close statistical rendering of spectral transmission (dashed line at bottom-left). Statistical *B* and *S* coefficients are refined (solid circles) by least-squares fitting the Malkmus transmission to line-by-line calculated transmission over a broad (***log* u**) absorber range. Bottom-right panels show how Malkmus *k*-distribution can be analytically converted to histogram form for any absorber amount, stacked vertically (as in a multi-layered atmosphere) to preserve the implicit spectral information. Results are compiled as a pressure, temperature, absorber amount look-up table that closely reproduces line-by-line accuracy at a small fraction of the computing cost.

**Slide 17** The thermal radiation emitted by Earth is view-angle dependent due to the vertical atmospheric temperature gradient. Clear-sky satellite nadir-view sees deepest into the atmosphere, and thus encounters the warmest along-site temperatures. Off-nadir radiances originate from higher altitudes and proportionately cooler temperatures. In the above, a cloud is placed at high near-tropopause altitude, and its optical depth is varied logarithmically from near-zero ($\tau$=0.01) to saturation ($\tau$=10). In the GISS GCM radiation code, LW radiances are calculated at three emission angle quadrature points (black dots). A numerical quadrature is then applied to obtain the angle integrated LW flux (red diamonds). Because of angle dependent transmission, clouds exert significant control over the angle dependence of outgoing radiation. The angle dependence (limb-darkening) is steepest for optically thin clouds ($\tau$=0.1), converting to limb-brightening for optically dense clouds.

Climate GCMs typically utilize a diffusivity approximation (heavy blue vertical line) when calculating LW fluxes. Overall, this a good approximation, but as shown in the right-hand panel, compared to angle-integrated flux, the diffusivity approximation produces LW flux biases of 3-4 $W/m^2$ for clouds in the cirrus $\tau$=0.1-1.0 range.

**Slide 18** Cloud scattering effects on LW fluxes are small, and they are usually ignored in climate modeling applications. However, given the three-quadrature point approach in LW flux calculation in the GISS GCM, a parameterized correction based on off-line calculations of the LW spectral cloud reflectivity and emissivity is possible and has been implemented. The parameterization includes spectral emissivity corrections for cloud emitted radiances and reflected radiance contributions at cloud top and at cloud bottom. The net effect of LW cloud scattering is a reduction in the outgoing (TOA) LW flux (top-right panel) by 1.4 $W/m^2$ on a global annual-mean basis, and an increase in the downwelling flux (bottom-right panel) at the ground surface (BOA) by 0.39 $W/m^2$.

LW scattering is more efficient for ice clouds because of their higher reflectivity in the 20-30 μm region. It is more pervasive at higher latitudes, coinciding broadly with the global cloud cover (top-left panel) and with high clouds (bottom-left panel). The downwelling flux correction is more evident in the drier polar regions. The LW cloud scattering enhances the cloud greenhouse effect by reducing the outgoing LW flux.

**Slide 19** Mie scattering imparts a unique polarimetric signature to every refractive index and particle size combination. First order scattering constitutes the "polarization angle spectrum" as a function of the Sun-particle-detector scattering angle that is uniquely characteristic for each (***nr***,***Reff***) combination. Successive orders of scattering tend to add mostly unpolarized intensity, so that the polarization imparted by the first order scattering remains readily identifiable in the observed radiance. When several (***nr***,***Reff***) combinations are present in the observed radiance, each contributor can be identified by its polarization angle spectrum similar to identifying gases by their spectral signatures. In the above Mie-scattering polarization grid, the refractive index increases vertically (***nr*** = 1.33, 1.43, 1.53 for water, sulfate, dust), and particle size increases horizontally (***Reff*** = 0.2, 1.0 μm for aerosol, and 5, 15 μm for cloud).

**Slide 20** Airborne Research Scanning Polarimeter (RSP) makes polarimetric and radiance intensity measurements at 410, 470, 555, 670, 865, 1590 and 2250 nm (blue, mauve, turquoise, green, red, magenta, black). Viewing geometry in the top-row panels is for a relative solar azimuth of 205°, and solar zenith of 62° for two different surface types. The spectral reflectances for the two surface types show significant variations in color and directionality. However, the *polarized* surface reflectance is smaller by two orders of magnitude, and it tends to be spectrally gray, being dependent instead on viewing geometry. As shown in the bottom-row panels, this circumstance makes it possible for combined polarimetry-intensity based analyses to retrieve accurate cloud and aerosol radiative properties compared to co-located AERONET ground-truth measurements, a capability that is not possible using intensity-only observational data.

Current intensity-only satellite data are unable to retrieve aerosol properties commensurate with AERONET ground-truth measurements because of their inability to differentiate light intensity from the ground surface, aerosol, or from sub-pixel cloud contamination. Polarimetry offers an additional capability to help resolve this retrieval ambiguity [*Mishchenko et al., 2007*].